CHEMISTRY OF MATERIALS

Article

pubs.acs.org/cm

# Stable Phosphorus-Enriched (0001) Surfaces of Nickel Phosphides

Robert B. Wexler, John Mark P. Martirez,[†] and Andrew M. Rappe*

The Makineni Theoretical Laboratories, Department of Chemistry, University of Pennsylvania, Philadelphia, Pennsylvania 19104-6323, United States

Supporting Information

**ABSTRACT:** In heterogeneous catalysis, catalyst synthesis precedes operation and, in most cases, is conducted in an altogether different chemical environment. Thus, determination of the structure and composition of the catalyst surface(s) due to fabrication is essential in accurately evaluating their eventual structure(s) during operation, which provides the origin of their catalytic activities and are therefore key to catalyst optimization. We explore the reconstructions of both $Ni_2P(0001)$ and $Ni_5P_4(0001)/(000\bar{1})$ surfaces with first-principles density functional theory (DFT). Most of the stable terminations under realistic synthesis conditions are determined to be P-rich on both materials. A P-covered reconstruction of the $Ni_3P_2$ termination of $Ni_2P(0001)$ is found to be most stable, consistent with the current literature. By contrast, the most energetically favorable surfaces of $Ni_5P_4$ are found to be the $Ni_3P_3$ and $Ni_4P_3$ bulk-derived terminations with P-adatoms. The preferred excess P binding sites and their energies are identified on each surface. We find that the $P_3$ site, which is present on $Ni_5P_4$, and the $Ni_3$ site, which is present on both $Ni_2P$ and $Ni_5P_4$, strongly bind excess P. Additionally, we predict the presence of stable $P_n$ ($n$ = 2, 4) agglomerates on $Ni_5P_4$ at the $P_3$-hollow and Ni−Ni bridge sites. This study highlights the importance of considering the aggregation behavior of nonmetal components in predicting the surface reconstruction of transition metal compounds.

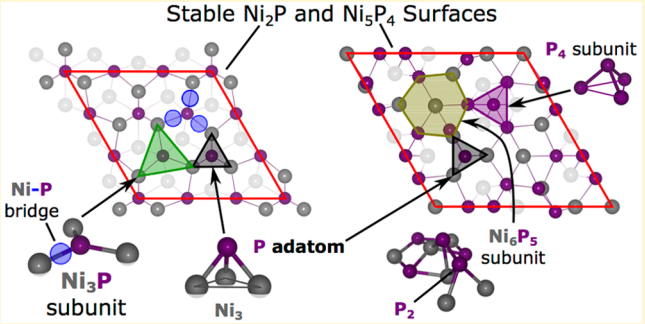


## INTRODUCTION

Elemental enrichment of the surfaces of transition metal oxides, sulfides, and phosphides is a desirable route to modify their physical and/or chemical properties. The ability to manipulate the amount of the transition metal component of a transition metal compound is believed to be the key to modifying the chemistry of its surface. Perhaps for oxides this is naively rooted in the fact that oxygen cannot stably form extended compounds or chains exceeding three atoms (*e.g.* ozone), and thus surfaces of oxides are most directly manipulated through their metallic components. Phosphorus and sulfur, however, can form extended chains or crystals on their own; thus P and S present possible sources of solid secondary phases when they form compounds with metals.[1−3] This behavior may have deeper implications for the types of stable surfaces metal phosphides or sulfides form.

Surface composition and structure govern the key catalytic properties of nickel phosphides for a number of industrially important chemical reactions.[4−8] The material properties of transition metal phosphides, including binary, ternary, and mixed-metal compounds, have been well characterized since the 1960s.[9,10] They form binary phosphides $M_xP_y$ (where $M$ denotes a transition metal) with compositions usually ranging from $M_3P$ to $MP_3$ including $Ni_2P$, $Ni_5P_4$, $Ni_3P$, $Ni_5P_2$, $Ni_{12}P_5$, NiP, and $NiP_2$.

The metal-rich phosphides ($M_xP_y$ where $x > y$) tend to exhibit better thermal stability, chemical inertness, electrical conductivity,[11−13] and hardness than P-rich phases; therefore we focus on $Ni_2P$ and $Ni_5P_4$ in this study. Both solids have hexagonal crystal structures, as shown in Figure 1. Their low index (0001) facets are found to be the most stable terminations for both compounds. $Ni_2P$ has two unique terminations on the (0001) plane, the $Ni_3P$ and $Ni_3P_2$ layers, and they have distinct structure and stoichiometry. DFT calculations reveal that the latter is more stable under conditions where bulk $Ni_2P$ is stable.[14] Calculated scanning tunneling microscope (STM) images for this termination[14] do not, however, match experimental data.[13,15,16] This apparent inconsistency was resolved by dynamic low-energy electron diffraction (LEED) experiments, which revealed a surface reconstruction where nonstoichiometric additional P covers the $Ni_3P_2$ surface at the $Ni_3$-hollow sites (see Figure 5 in ref 27). They showed that this P-covered $Ni_3P_2$ termination (hereafter denoted as $Ni_2P{-}Ni_3P_2{+}P$) comprises ∼80% of the surface, whereas the $Ni_3P_2$ (hereafter denoted as $Ni_2P{-}Ni_3P_2$) makes up the remaining 20%. Other reconstructions have been reported but only after annealing at higher temperatures, *e.g.*, above 790 K.[15,17] By contrast, $Ni_5P_4$ has a larger unit cell composed of $Ni_3P_2$, $Ni_3P_3$, and $Ni_4P_3$ layers (Figure 1b). Additionally, $Ni_5P_4$ lacks reflection symmetry with respect to

Received: April 11, 2016
Revised: July 11, 2016
Published: July 18, 2016






DOI: 10.1021/acs.chemmater.6b01437
Chem. Mater. 2016, 28, 5365−5372

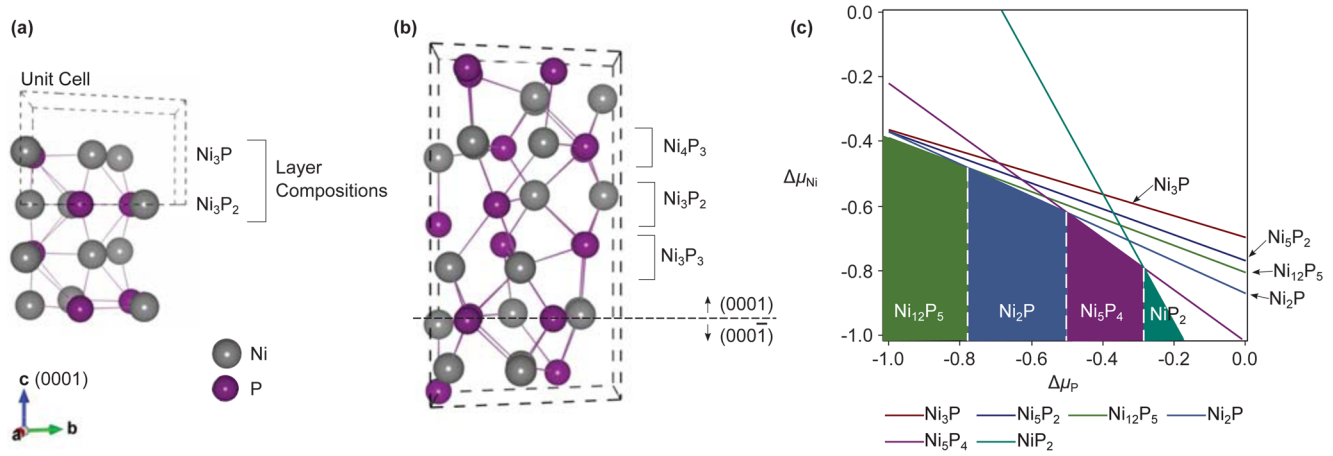


**Figure 1.** Crystal structures of (a) $Ni_2P$ and (b) $Ni_5P_4$, highlighting the layer stacking along the [0001] direction. (c) Bulk phase diagram as a function of the relative chemical potentials (eV) of Ni and P for nickel phosphide phases that are stable under 850 K as has been found in the literature. Each solid line satisfies the equilibrium equation: $\Delta G_{Ni_xP_y} = x\Delta\mu_{Ni} + y\Delta\mu_P$ at 0 K. Each dotted vertical line denotes a phase coexistence point.

the [0001] plane. The surface structures of $Ni_5P_4$ have not been studied previously. Although both are demonstrated to be efficient catalysts for $H_2$ evolution, $Ni_5P_4$ is much more active than $Ni_2P$, thereby igniting interest in the differences and similarities of these surfaces with the hope of elucidating their hydrogen evolution reaction (HER) catalytic activities.[8]

In this work, we conduct a comprehensive, systematic theoretical investigation of surface reconstruction on the (0001) and (000$\bar{1}$) facets of $Ni_2P$ and $Ni_5P_4$. First, we calculate the standard energy of formation for different bulk nickel phosphides ($Ni_xP_y$) with first-principles calculations so as to determine the region of P chemical potential ($\Delta\mu_P$) where bulk $Ni_2P$ and $Ni_5P_4$ are stable. Then, we compute the free energy for a large number of distinct surface terminations. We show that both $Ni_2P$(0001) and $Ni_5P_4$(0001) prefer chemical and structural reconstructions of their bulk terminations, thereby providing a framework for the re-examination of the HER mechanism on these nickel phosphides.

## COMPUTATIONAL METHODS

DFT[18,19] calculations with periodic boundary conditions are performed using the Quantum ESPRESSO code.[20] The generalized gradient approximation (GGA) is employed to calculate the exchange-correlation energy using the method of Perdew, Burke, and Ernzerhof (PBE).[21] Optimized,[22] norm-conserving, designed nonlocal[23] pseudopotentials were generated using OPIUM[24] to represent the core electrons and soften the potential for the valence electron wavefunctions. Semicore 3p states are treated along with the 4s, 4p, and 3d for Ni, while 3s, 3p, and 3d valence states are included for P. The 3d orbitals of P are deemed necessary to model anionic electron configurations and complex coordination environments. The valence states are expanded in a plane-wave basis with a 50 Ry kinetic energy cutoff. For bulk calculations, 5 × 5 × 6 and 5 × 5 × 4 $k$-point grids, shifted along $k_z$, are used to sample the Brillouin zones of $Ni_2P$ and $Ni_5P_4$, respectively, and a small (0.005 Ry) Gaussian electronic smearing is applied to improve electronic convergence. All cells are allowed to fully relax, with a stress convergence threshold of 0.01 kbar. We perform spin-polarized calculations for bulk $Ni_2P$ and $Ni_5P_4$. The spin configuration is initially ferromagnetic, but both systems relax to a nonferromagnetic state.

Surfaces are modeled using slabs with 1 × 1 (for high surface defect concentrations) and $\sqrt{3} \times \sqrt{3}$ $R30°$ (for fractional defect concentrations) surface cells separated by ∼15 Å of vacuum. For slabs, the $k$-point grid sampling is reduced to 5 × 5 × 1 and 3 × 3 × 1, respectively. Orbital-projected density of states (DOS) calculations and Löwdin population analysis are performed on the stable surface reconstructions of $Ni_2P$ and $Ni_5P_4$ using a finer $k$-point grid (12 × 12 × 1). A dipole correction[25] is applied to further remove the artificial electric field interactions between periodic images; its contribution to the total energy, however, is very small. We consider the (0001) surface of both $Ni_2P$ and $Ni_5P_4$. Seven-layer, up−down symmetric slabs are used to model $Ni_2P$(0001) terminations. For $Ni_5P_4$, asymmetric slabs of thickness ranging from 10 to 12 layers are constructed. In studying the reconstructions of the (0001) surface of $Ni_5P_4$, the composition of the (000$\bar{1}$) is kept to be $Ni_4P_3$. Likewise, in studying (000$\bar{1}$), the same type of termination is kept for (0001). All atoms are allowed to fully relax with a force convergence threshold of $10^{-3}$ Ry/Bohr.

The surface free energy ($\Omega$) is calculated under various environmental conditions using the following expression:

$$\Omega = \frac{1}{2A}(\phi + \Gamma_P\Delta\mu_P) \quad (1)$$

where $A$ is the area of the surface unit cell, $\Delta\mu_P$ is the chemical potential of phosphorus relative to bulk phase white phosphorus, and $\phi$ and $\Gamma_P$ are

$$\phi = E_{slab} - \frac{N_{Ni}E^{bulk}_{Ni_xP_y}}{x} + \Gamma_P E^{bulk}_P \quad (2)$$

$$\Gamma_P = N_{Ni}(y/x) - N_P \quad (3)$$

Here, $E_{slab}$ is the DFT total energy of the slab, $N_{Ni/P}$ is the number of Ni/P atoms in the slab, $x/y$ is the number of Ni/P atoms per formula unit of the bulk, and $E^{bulk}$ is the formation energy of the bulk compound in the subscript. Equation 1 is governed by the equilibrium conditions defined by the dominant bulk phase and a secondary P chemical reservoir.

## RESULTS AND DISCUSSION

**Bulk Stability of $Ni_2P$ and $Ni_5P_4$.** A prerequisite of the existence of a surface is the presence of a stable bulk phase that supports it. Thus, to be able to determine the chemical potential ranges where certain surfaces become relevant, we generate a bulk phase diagram from first-principles thermodynamic calculations (Figure 1c). Another P-rich phase, NiP, is expected to dominate in the same P chemical potential range as $NiP_2$. However, NiP was demonstrated to only appear at high temperatures (>850 K)[26] and thus was not included in the


DOI: 10.1021/acs.chemmater.6b01437
Chem. Mater. 2016, 28, 5365−5372

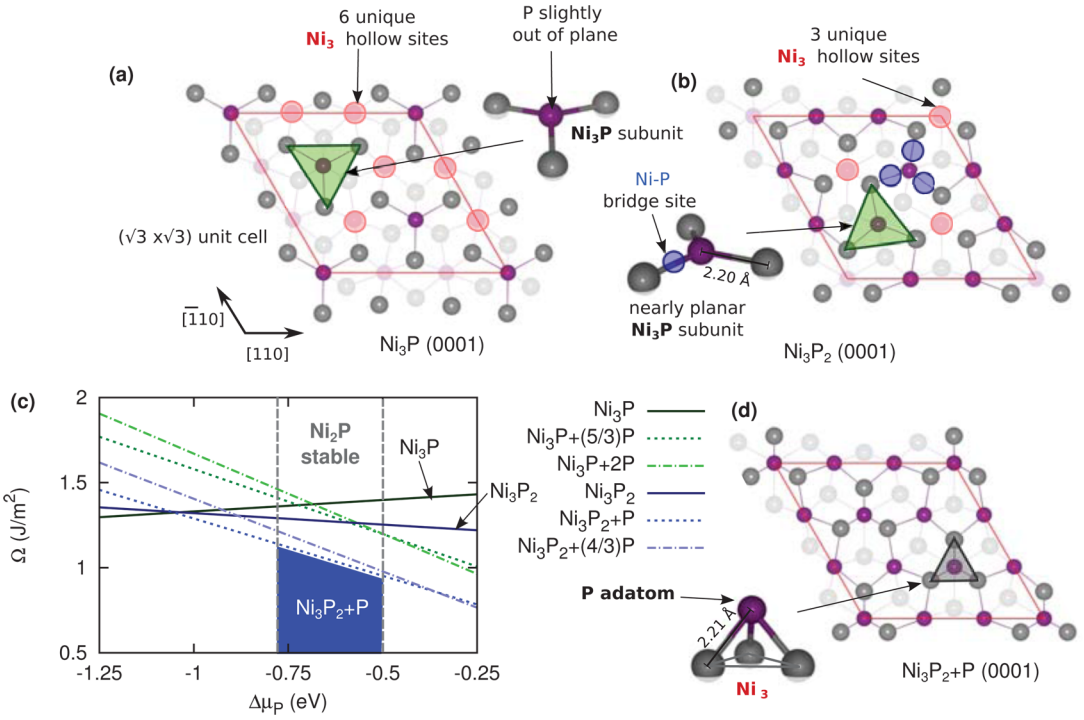


**Figure 2.** Surface crystal structures of $Ni_2P(0001)$ with either a (a) $Ni_3P$ or (b) $Ni_3P_2$ termination. Only the atoms of the outermost layers are clearly shown. Structural insets highlight the basic subunits of each surface. Red lines outline the $\sqrt{3}\times\sqrt{3}\ R\ 30°$ supercells. (c) Surface phase diagram for $Ni_2P(0001)$ as a function of $\Delta\mu_P$ (eV). Surface energies are reported in J/m$^2$. Dashed gray vertical lines border the bulk stability region for $Ni_2P$.

phase diagram (Figure 1c), which represents only low temperature conditions since we neglect entropy contributions. It shows the values of $\Delta\mu_P$ and $\Delta\mu_{Ni}$ where bulk $Ni_2P$ and $Ni_5P_4$ are stable compared to other nickel phosphide compositions. We find that $Ni_2P$ is stable at $-0.78\ \text{eV} \le \Delta\mu_P \le -0.50\ \text{eV}$. At $\Delta\mu_P = -0.50$ eV, bulk $Ni_5P_4$ becomes thermodynamically favored up to $\Delta\mu_P = -0.28$ eV, at which point bulk $NiP_2$ becomes favored. The regions where these two phases are stable define the chemical potentials where their respective surfaces and their corresponding reconstructions are bound to exist. These surface reconstructions are discussed in the following sections.

**Surface Structure and Stability of $Ni_2P(0001)$.** First, we describe the bulk-derived terminations of $Ni_2P(0001)$. As shown in Figure 1a, bulk $Ni_2P$ has two distinct layer compositions along the *c*-axis, $Ni_3P$ and $Ni_3P_2$, where two layers constitute a unit cell. The surface crystal structure of $Ni_2P{-}Ni_3P$ is shown in Figure 2a for a $\sqrt{3}\times\sqrt{3}\ R\ 30°$ surface unit cell. The outermost layer consists of repeating $Ni_3P$ subunits (green shaded triangle) with the central P sticking slightly out of the surface plane (shown in the inset). This surface also possesses six unique $Ni_3$ hollow sites (red shaded circles), which are formed by the Ni corners of the $Ni_3P$ subunits. $Ni_3P$ subunits are also found on $Ni_2P{-}Ni_3P_2$ but adopt a geometry where the central P is nearly coplanar with the Ni corners (see Figure 2b). Owing to the increased surface P concentration on this termination, the number of unique $Ni_3$ hollow sites reduces to three. The center of the $Ni_3P$ subunits in the $Ni_2P{-}Ni_3P$ layer are above (and below) the $Ni_3$ hollows of the $Ni_2P{-}Ni_3P_2$ and *vice versa*. This stacking arrangement reveals a $Ni_3P{-}Ni_3$ pattern along the [0001] direction. The surface energy of $Ni_2P{-}Ni_3P$ and $Ni_2P{-}Ni_3P_2$ is plotted in Figure 2c as a function of $\Delta\mu_P$. In the bulk $Ni_2P$ stability region, $Ni_2P{-}Ni_3P_2$ is the preferred bulk-like termination, which is consistent with previous DFT calculations in the literature.[14]

Given that there is experimental evidence for P-enrichment of $Ni_2P$ surfaces,[13,15,16,27,28] we investigate the possibility of stabilizing bulk terminations by systematically adding extra P to the surface and then identify the most stable reconstruction. We find that the adsorption of P at $Ni_3$ hollow sites in a trigonal pyramidal geometry decreases the surface free energy of both $Ni_2P{-}Ni_3P$ and $Ni_2P{-}Ni_3P_2$ (see Figure 2c). This particular binding site and geometry is expected because it is analogous to creating a new, partial layer with P at bulk lattice positions. It is also different than the $Ni_3P$ subunit, which has a nearly planar geometry. The Ni-rich (P-poor) $Ni_2P{-}Ni_3P$ termination is maximally stabilized by the addition of P at five out of the six $Ni_3$ hollow sites to generate a surface composition of $Ni_3P{+}(5/3)P$ (defect concentration denoted per $1\times1$ surface unit cell). Higher coverages through further adsorption of P at the sixth $Ni_3$ hollow site ($Ni_2P{-}Ni_3P{+}2P$) causes the surface free energy to slightly increase, signaling P saturation. For $Ni_2P{-}Ni_3P_2$, the surface energy is minimized by the addition of P at all three $Ni_3$ hollow sites ($Ni_3P_2{+}P$ in Figure 2d). If a fourth P is added to make $Ni_2P{-}Ni_3P_2{+}(4/3)P$, it binds to a Ni–P bridge site, forms a surface adsorbed $P_2$ complex with P from the nearest $Ni_3$ hollow site (see Figure S1 in the Supporting Information), and increases the surface energy. Comparing the surface energies of both bulk-like terminations and their reconstructions, $Ni_2P{-}Ni_3P_2{+}P$ is the most stable surface phase whenever bulk $Ni_2P$ is stable, *i.e.*, under relatively P-rich conditions. Thus, for a thermodynamically controlled synthesis of $Ni_2P$, this surface should be the most prevalent phase and, in fact, it is the same structure that ref 27 predicts, which they found to be the most consistent with the experimental STM among the surfaces they investigated.



DOI: 10.1021/acs.chemmater.6b01437
*Chem. Mater.* 2016, 28, 5365−5372

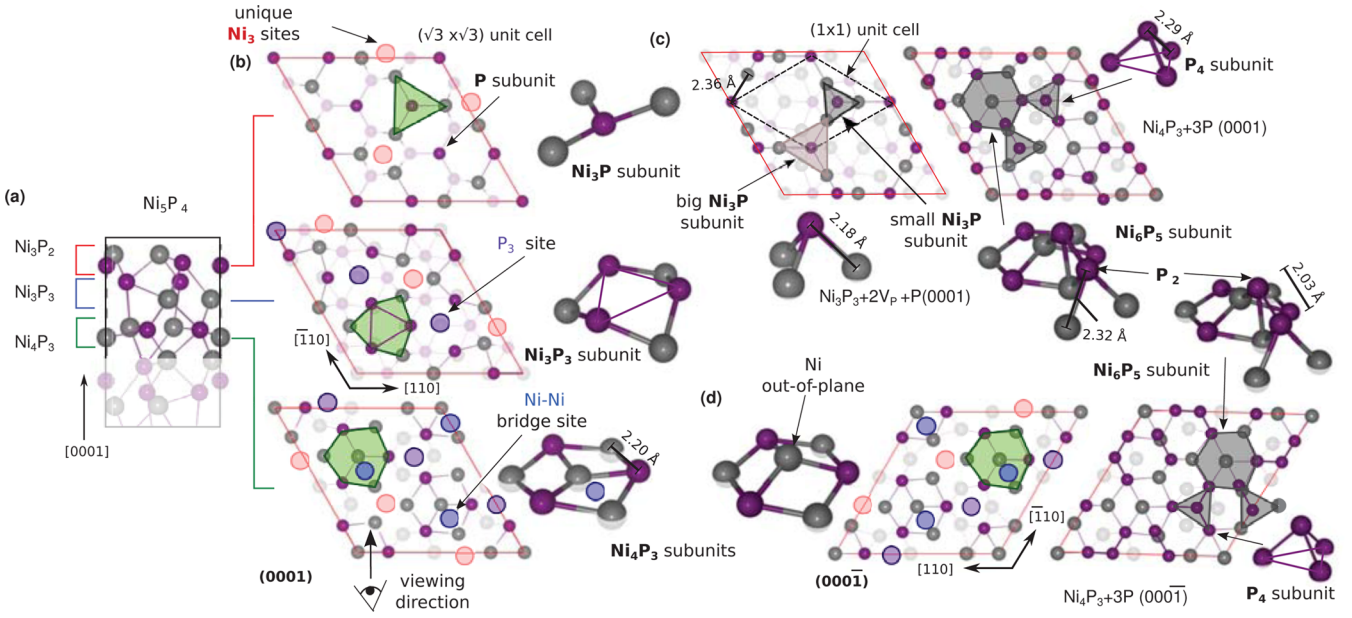


**Figure 3.** Surface crystal structure for bulk-derived terminations and reconstructions of $Ni_5P_4(0001)$ and $(000\bar{1})$. (a) Bulk layering in $Ni_5P_4$. (b) Bulk-like (0001) terminations $Ni_3P_2$ (top), $Ni_3P_3$ (middle), and $Ni_4P_3$ (bottom) with shaded regions corresponding to the insets highlighting important structural features. (c) Stable (0001) reconstructions $Ni_5P_4$–$Ni_3P_3$+2$V_P$+P (left) and $Ni_5P_4$–$Ni_4P_3$+3P (right). (d) Bulk-like (left) and reconstructed (right) $Ni_5P_4$–$Ni_4P_3$+3P$(000\bar{1})$.

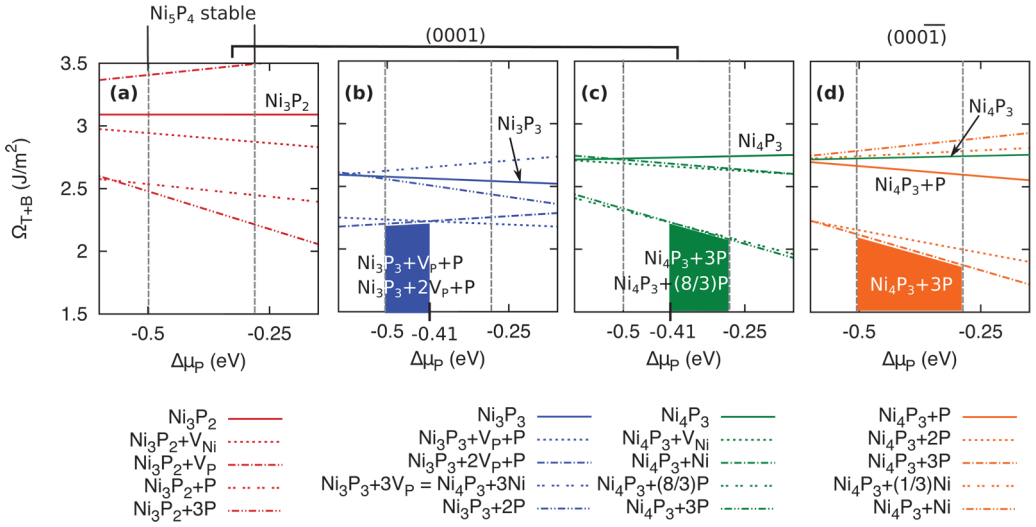


**Figure 4.** Surface phase diagram for $Ni_5P_4(0001)$ and $(000\bar{1})$ surfaces as a function of $\Delta\mu_P$ (eV). $\Omega_{T+B}$ corresponds to the combined surface energies (J/m$^2$) of the top (T) and bottom (B) surfaces of (a) $Ni_3P_2(0001)$, (b) $Ni_3P_3(0001)$, (c) $Ni_4P_3(0001)$, and (d) $Ni_4P_3(000\bar{1})$ and their respective reconstructions. Shaded areas denote regions of $\Delta\mu_P$ where certain reconstructions (as labeled) are favored.

The presence of P adatoms in $Ni_3$-hollow sites on the reconstruction $Ni_2P$–$Ni_3P_2$+P has important implications for the catalytic activity of $Ni_2P(0001)$ toward HER. It was proposed that H can adsorb at both $Ni_3$-hollow and Ni–P bridge sites, where the latter offers more moderate binding.[29] H atoms at these two sites can diffuse to one another and subsequently desorb, forming $H_2(g)$. Adlayer P offers a new site for H adsorption while also blocking the conventional bulk-like $Ni_3$ sites, thereby prompting a reconsideration of the HER mechanism on $Ni_2P(0001)$.[30] $Ni_3$-hollow sites play a key role in the predicted mechanisms of other important chemical reactions such as hydrodesulfurization (HDS),[31,32] water–gas shift (WGS),[6] and hydrodeoxygenation (HDO).[33] Their catalytic mechanisms should be revisited on reconstructed $Ni_2P(0001)$ surfaces since the above analysis shows that $Ni_3$-hollow sites may not in fact be readily available.

**Surface Structure and Stability of $Ni_5P_4(0001)$ and $(000\bar{1})$.** As mentioned above, $Ni_5P_4$ lacks mirror symmetry along [0001], giving rise to structurally distinct (0001) and $(000\bar{1})$ surfaces. Additionally, the structural layers of $Ni_5P_4$ are less clearly delineated. We choose to decompose the structure into three layers and refer to them according to their formula unit: $Ni_3P_2$, $Ni_3P_3$, and $Ni_4P_3$ (Figure 3a). A set of three layers forms half a unit cell, where the addition of a second set of three layers that are rotated 180° about the (0001) axis completes the full unit cell. Note that due to the absence of a reflection symmetry about the [0001], the layer that comes before a given layer along the [0001] becomes the layer that


DOI: 10.1021/acs.chemmater.6b01437
Chem. Mater. 2016, 28, 5365–5372

comes after along the $[000\bar{1}]$. For example the layer below the $Ni_5P_4$–$Ni_3P_2(0001)$ surface is the $Ni_5P_4$–$Ni_3P_3$ layer, whereas the layer below the $Ni_5P_4$–$Ni_3P_2(000\bar{1})$ is the $Ni_5P_4$–$Ni_4P_3$ layer. Therefore, the absence of reflection symmetry means different subsurface layers, which will affect the chemistry of the (0001) vs. $(000\bar{1})$ surface layer, despite having the same composition.

For brevity, we only discuss here in detail the structural and chemical features of the (0001) surfaces and their reconstructions, while the $(000\bar{1})$ layer that produces the most stable reconstruction is discussed. We discuss each bulk-derived layer and the different structural and compositional perturbations giving rise to their reconstructions. The compositional variations introduced include Ni vacancies ($V_{Ni}$), P vacancies ($V_P$), P adatoms (+*x*P, as in the $Ni_2P$ surface reconstructions), and Ni adatoms (+*x*Ni). We also discuss the energetics involved in these reconstructions, revealing the most likely (thermodynamically stable) surfaces of $Ni_5P_4(0001)$.

*$Ni_3P_2$-Derived Surfaces of $Ni_5P_4$.* The upper panel of Figure 3b shows the $(\sqrt{3} \times \sqrt{3})R\ 30°$ (three unit cells) of the bulk-derived $Ni_5P_4$–$Ni_3P_2$ layer. This layer is composed of repeated $Ni_3P$ (green shaded triangle) and P subunits. Each isolated P subunit is coordinated to three P atoms found in the layer below. The removal of this lattice P, creating vacancies ($V_P$), is unfavorable and destabilizes the surface (Figure 4a, compare solid line, $Ni_5P_4$–$Ni_3P_2$, and dash-dotted line, $Ni_5P_4$–$Ni_3P_2$+$V_P$). The corners of three adjacent $Ni_3P$ units surround a common point, which creates a $Ni_3$ hollow site (red shaded circle). Removal of one of these Ni atoms somewhat stabilizes the surface by about 0.25 J/m$^2$ ($Ni_5P_4$–$Ni_3P_2$+$V_{Ni}$, dotted line), while saturating all the $Ni_3$ hollow sites with one and up to three P per site, creating a $P_3$ staggered against the $Ni_3$, ($Ni_5P_4$–$Ni_3P_2$+(1,3)P, double dotted and dash-double dotted lines, Figure 4) stabilizes the surface significantly more (≈0.5–0.75 J/m$^2$).

*$Ni_3P_3$-Derived Surfaces of $Ni_5P_4$.* The middle panel of Figure 3b shows the $\sqrt{3} \times \sqrt{3}\ R\ 30°$ $Ni_5P_4$–$Ni_3P_3$ layer. Closed-chain $Ni_3P_3$ subunits compose this surface. The $Ni_3P_3$ subunit is characterized by a triangular $P_3$ overlaid on a $Ni_3$ that are rotated 60° relative to each other. The Ni corners of three $Ni_3P_3$ subunits also converge on a common point which also creates a trinuclear Ni hollow site (red shaded circles). The same is true for the three P corners which correspondingly create a trinuclear P hollow site (purple shaded circles). As in the $Ni_5P_4$–$Ni_3P_2$ surface, saturation of these $Ni_3$ and $P_3$ sites with one P per site stabilizes this surface. Figure 4b shows the stabilizing effect of saturating both the $Ni_3$ and $P_3$ sites (solid, $Ni_5P_4$–$Ni_3P_3$ vs dash-double dotted line, $Ni_5P_4$–$Ni_3P_3$+2P). However, saturating the $Ni_3$ sites alone and removing one of the lattice P's ($Ni_5P_4$–$Ni_3P_3$+$V_P$+P) better stabilizes the surface, with one of the remaining P's displaced toward the center of the $Ni_3P_2$ subunit (see Figure S2 in the Supporting Information). The removal of another P from the $Ni_3P_3$ subunit further lowers the surface energy in the low $\Delta\mu_P$ regime (dotted line, $Ni_5P_4$–$Ni_3P_3$+2$V_P$+P) and exhibits the same displacement of the remaining P to the center of the $Ni_3$ base, creating a big $Ni_3P$ subunit (Figure 3c, left panel). The $n$$V_P$+P where ($n$ = 1–2) stabilizes the surface by ~0.25 J/m$^2$, making these the most stable reconstructions of the $Ni_5P_4$–$Ni_3P_3$ layer. The dominance of these surfaces is made possible by a combination of low P chemical potential and the tendency of the system to maximize the number of Ni–P bonds.

*$Ni_4P_3$-Derived Surfaces of $Ni_5P_4$.* The bottom panel of Figure 3b shows the $\sqrt{3} \times \sqrt{3}\ R\ 30°$ $Ni_5P_4$–$Ni_4P_3$ layer. This layer is composed of $Ni_4P_3$ subunits with the same motif as the $Ni_3P_3$ subunits found in the $Ni_5P_4$–$Ni_3P_3$ layer, but with an additional Ni at the center. Also, similar to the $Ni_5P_4$–$Ni_3P_3$ layer, the subunits create $Ni_3$ (red shaded circles) and $P_3$ (purple shaded circles) hollow sites (one of each per 1 × 1 surface). However, the extra Ni, which makes this layer distinct from the $Ni_5P_4$–$Ni_3P_3$, gives rise to Ni–Ni bridge sites (blue shaded circle). Both Ni vacancies ($V_{Ni}$) and Ni adatoms (+Ni), marginally stabilize the surface. Saturation with P adatoms of all the $Ni_3$ and $P_3$ sites and one Ni–Ni bridge site per $Ni_4P_3$ subunit ($Ni_5P_4$–$Ni_4P_3$+3P) proved to be the most thermodynamically favorable. Partial occupation of the Ni–Ni bridge site may also be achieved, *e.g.*, in the case of $Ni_5P_4$–$Ni_4P_3$+(8/3)P. The structure of P-saturated $Ni_5P_4$–$Ni_4P_3$ ($Ni_5P_4$–$Ni_4P_3$+3P) is shown in the right panel of Figure 3c. A distinctive tetrahedral $P_4$ subunit forms from the adsorption of P at the $P_3$ site, while a $P_2$ moiety is stabilized from the bonding of the two P adatoms on a Ni–Ni bridge and a $Ni_3$ site.

*Global Stability of the (0001) Reconstructions of $Ni_5P_4$.* Bulk $Ni_5P_4$ was calculated to be stable between $\Delta\mu_P$ −0.5 and −0.28 eV, so we examine the surfaces with the lowest surface energy within this range. The $Ni_5P_4$–$Ni_3P_3$-derived surface with either the 2$V_P$+P or $V_P$+P reconstruction is found to be the most stable (0001) termination from $\Delta\mu_P$ −0.5 to −0.41 eV (blue shaded region in Figure 4b). At a higher $\Delta\mu_P$, −0.41 to −0.28 eV, the P-covered $Ni_5P_4$–$Ni_4P_3$-derived surfaces, $Ni_5P_4$–$Ni_4P_3$+3P and $Ni_5P_4$–$Ni_4P_3$+8/3)P, dominate (green shaded region in Figure 4c).

*$Ni_5P_4(000\bar{1})$ Reconstructions.* Despite the change in the sublayer composition supporting each termination (due to the change of the layer sequence when going the opposite direction), the $(000\bar{1})$ surface is found to be also thermodynamically dominated by the P-covered $Ni_5P_4$–$Ni_4P_3$-derived surfaces. The $Ni_5P_4$–$Ni_4P_3(000\bar{1})$ exhibits the same sites as the $Ni_5P_4$–$Ni_4P_3(0001)$, i.e. $Ni_3$ and $P_3$ hollow and Ni–Ni bridge sites, and is similarly composed of the $Ni_4P_3$ subunit (Figure 3d, left panel). The difference between the (0001) and $(000\bar{1})$ surfaces is the direction of the corrugation of central Ni of the subunits. The central Ni points into the slab in the case of the (0001), while it points outward to the vacuum in the case of the $(000\bar{1})$. Full saturation of the hollow sites and one Ni–Ni bridge site per $Ni_4P_3$ subunit ($Ni_5P_4$–$Ni_4P_3$+3P) also ultimately stabilizes this surface, in fact dominating the whole stability region of $Ni_5P_4$ (Figure 4d). The compositional and structural similarity of the most stable reconstructions of these (0001) and $(000\bar{1})$ surface isomers may render the two surfaces indistinguishable without the knowledge of the stacking direction within the bulk. However, at slightly lower P concentrations ($\Delta\mu_P$ < −0.41 eV), the (0001) undergoes a phase change into $Ni_5P_4$–$Ni_3P_3$+2$V_P$+P, while the $(000\bar{1})$ robustly remains as $Ni_5P_4$–$Ni_4P_3$+3P. See Supporting Information for a complete survey of the $(000\bar{1})$ layers and reconstructions.

**Comparison of the Stable $Ni_2P$ and $Ni_5P_4$ (0001) Reconstructions.** We have shown that the enrichment of $Ni_2P$ and $Ni_5P_4$ (0001) and $(000\bar{1})$ surfaces with P has a significant stabilizing effect. The most stable reconstruction for $Ni_2P(0001)$ is the $Ni_3P_2$+P surface, which has an overall composition of $Ni_3P_3$ and a 1:1 ratio of Ni to P. The preferred reconstructions for $Ni_5P_4$ (0001) and $(000\bar{1})$, namely $Ni_3P_3$+[1–2]$V_P$+P and $Ni_4P_3$+[(8/3)-3]P, are where Ni/P


DOI: 10.1021/acs.chemmater.6b01437
Chem. Mater. 2016, 28, 5365–5372

varies from 0.66 to 1.5. The reconstructions of $Ni_2P$ and $Ni_5P_4$ similarly exhibit P adsorption at $Ni_3$ hollows to generate a $Ni_3P$ trigonal pyramid, the only difference being the number of $Ni_3$ hollow sites per unit area and the Ni−P bond distance (see Figures 2 and 3). Unlike $Ni_2P$ reconstructions, however, $Ni_5P_4$−$Ni_4P_3$+3P (0001) and (000$\bar{1}$) promote the formation of stable aggregates of P on their surfaces, such as $P_4$ subunits and $P_2$ moieties. The former closely resembles the tetrahedral $P_4$ structures in P (s, white), has a very similar P−P bond distance ($d_{P(s)}$ = 2.21 Å[34] vs $d_{Surf}$ = 2.29 Å), and carries a nearly neutral charge (0.07*e*, Table 1), suggesting the possible nucleation of a secondary pure P phase. The $P_2$ moiety ($d_{Surf}$ = 2.03 Å) has a similar bond length to gaseous $P_2$ ($d_{P_2(g)}$ = 1.89 Å)[35] and also possesses nearly neutral charge (−0.05*e*, Table 1).

**Table 1. Calculated Löwdin Charges for the Surface P Atoms for Some of the Stable Reconstructions of $Ni_2P$ and $Ni_5P_4$**

| composition | | | no. electrons | | | net charge |
|---|---|---|---|---|---|---|
| bulk | surface | location | 3s | 3p | 3d | [*e*] |
| $Ni_2P$ | $Ni_3P_2$+P | $Ni_3P$ subunit | 1.60 | 3.19 | 0.88 | −0.68 |
| | | $Ni_3$-hollow | 1.75 | 3.09 | 0.48 | −0.30 |
| $Ni_5P_4$(0001) | $Ni_4P_3$+3P | $Ni_4P_3$ subunit | 1.46 | 3.06 | 1.09 | −0.61 |
| | | $Ni_3$-hollow | 1.55 | 3.05 | 0.72 | −0.32 |
| | | $P_3$-hollow | 1.55 | 2.77 | 0.61 | 0.07 |
| | | Ni−Ni bridge | 1.63 | 2.93 | 0.49 | −0.05 |

From the dominant structures, we see that the major driving force for the P-rich reconstruction is to saturate Ni coordination where it achieves either a four-fold or five-fold coordination as in the bulk. The complexity of the $Ni_5P_4$ reconstructions, especially the $Ni_4P_3$+3P surface composition, presents other avenues for surface stabilization which include the expansion of surface P valency through bonding with additional P, *e.g.*, at $P_3$ hollow sites. P−P bonds may act as possible nucleation centers for white P, $P_2$(g), and other P phases depending on the environmental conditions.

Unlike transition metal oxides which are more strongly ionic and whose surface reconstructions are governed by surface charge passivation,[36−38] the metallic nickel phosphides are demonstrated to be primarily driven by saturation of the coordination chemistry of the surface atoms. Due to the much greater electronegativity of O compared to P, transition metal oxides also tend to have larger bond dipoles than $Ni_2P$ and $Ni_5P_4$. Thus, at oxide surfaces, dangling bonds lead to the buildup of a large surface dipole, which can be screened by reconstruction with the constituent elements of the material or by cations or anions readily available in the environment.[39−41] The geometry of oxide and phosphide reconstructions is also affected by their electron configurations. Since O has a lower valence than P, oxide reconstructions tend to involve O adatoms bridging between two metal atoms or forming coordinatively unsaturated sites,[42] whereas P may easily form three bonds using its 3p orbitals while also expanding its valence shell using its energy-accessible 3d orbitals. On this basis, P can introduce modes of coordination beyond sp bonding. This is clearly demonstrated by the partial population of the P 3d orbitals (see Table 1 for the 3d charge population) and their hybridization with the P 3p states (see Figure S5 in the Supporting Information for the projected density of states of some of the surfaces). Such flexibility in valence enables the formation of exotic surface structures including small covalent P clusters.

Because bulk-like terminations of $Ni_2P$ and $Ni_5P_4$ tend to reconstruct, the previously proposed mechanism of HER[29,30] on $Ni_2P$ and $Ni_5P_4$, as well as other chemical reactions[6,31−33] for which it is catalytically active, must be reevaluated. Depending on the chemical reaction catalyzed, the catalyst may be subsequently exposed to different solvents, ions, molecules, and even applied potentials during operation which would then facilitate further evolution of the surfaces. Here, we provide a set of chemically sound structures that lay the foundation for studying the effects of these additional variables on catalysis. A few of the most notable routes for additional reconstructions to consider are perhaps through hydration, protonation, and hydroxylation of surface Ni and P species once exposed to water. We show however that the non-stoichiometric P ad-species prevalent on these reconstructions already constitute strong Ni-bond-passivating components of the surface. This suggests that P redox and acid−base chemistries (instead of nickel's) are more relevant in determining the eventual transformation and activity of the surfaces during catalysis. Thus, for example, phosphine and phosphorous/phosphoric acid chemistries may very well hold the key in understanding Ni−P catalysis in an aqueous environment.

## CONCLUSIONS

Both $Ni_2P$ and $Ni_5P_4$ favor P-rich reconstructions on the (0001) facet, arising from the extended coordination of P and the tendency of Ni to remain saturated. For $Ni_2P$, the most stable surface termination is $Ni_3P_2$+P, where P adatoms rest on the $Ni_3$-hollow sites. On $Ni_5P_4$(0001), reconstructions of both the $Ni_3P_3$ and $Ni_4P_3$ surface layer compositions may form. For its (000$\bar{1}$), $Ni_5P_4$−$Ni_4P_3$+3P is most stable. $Ni_5P_4$−$Ni_4P_3$+3P-(0001) and (000$\bar{1}$) are furnished by stable P clusters, $P_4$ and $P_2$, which resemble phases of P, namely white P and $P_2$(g), respectively. The ability of P to agglomerate on $Ni_5P_4$(0001) sets this phase apart from $Ni_2P$(0001) and, more generally, from transition metal oxides, which are much more limited in their modes of reconstruction and more adherent to surface charge passivation requirements.

## ASSOCIATED CONTENT

### Supporting Information

The Supporting Information is available free of charge on the ACS Publications website at DOI: 10.1021/acs.chemmater.6b01437.

Calculated bulk parameters, surface crystal structures of $Ni_2P$−$Ni_3P_2$+(4/3)P and $Ni_5P_4$−$Ni_3P_3$+$V_P$+P(0001), survey of the $Ni_5P_4$(000$\bar{1}$) layers and reconstructions, and calculated Löwdin charges and orbital-projected density of states (PDOS) for the surface atoms for the stable surface reconstructions and some of the bulk-derived terminations of $Ni_2P$ and $Ni_5P_4$(0001) and (000$\bar{1}$) (PDF)

## AUTHOR INFORMATION

### Corresponding Author

*E-mail: rappe@sas.upenn.edu.



DOI: 10.1021/acs.chemmater.6b01437
*Chem. Mater.* 2016, 28, 5365−5372

**Present Address**

[†]Department of Mechanical and Aerospace Engineering, Princeton University, Princeton, NJ 08544, USA

**Notes**

The authors declare no competing financial interest.

## ■ ACKNOWLEDGMENTS

R.B.W. acknowledges support from the Department of Energy, Division of Basic Energy Sciences, under grant DE-FG02-07ER15920. J.M.P.M. acknowledges support from the Office of Naval Research, under grant N00014-12-1-1033. A.M.R. acknowledges support from the National Science Foundation, under grant CMMI-1334241. The authors also acknowledge computational support from the High-Performance Computing Modernization Office and the National Energy Research Scientific Computing Center.

## ■ REFERENCES

(1) Haga, K.; Shiratori, Y.; Nojiri, Y.; Ito, K.; Sasaki, K. Phosphorus Poisoning of Ni-Cermet Anodes in Solid Oxide Fuel Cells. *J. Electrochem. Soc.* **2010**, *157*, B1693−B1700.

(2) Colletti, L. P.; Teklay, D.; Stickney, J. L. Thin-Layer Electrochemical Studies of the Oxidative Underpotential Deposition of Sulfur and its Application to the Electrochemical Atomic Layer Epitaxy Deposition of CdS. *J. Electroanal. Chem.* **1994**, *369*, 145−152.

(3) Meissner, D.; Benndorf, C.; Memming, R. Photocorrosion of Cadmium Sulfide: Analysis by Photoelectron Spectroscopy. *Appl. Surf. Sci.* **1987**, *27*, 423−436.

(4) Popczun, E. J.; McKone, J. R.; Read, C. G.; Biacchi, A. J.; Wiltrout, A. M.; Lewis, N. S.; Schaak, R. E. Nanostructured Nickel Phosphide as an Electrocatalyst for the Hydrogen Evolution Reaction. *J. Am. Chem. Soc.* **2013**, *135*, 9267−9270.

(5) Oyama, S. T. Novel Catalysts for Advanced Hydroprocessing: Transition Metal Phosphides. *J. Catal.* **2003**, *216*, 343−352.

(6) Liu, P.; Rodriguez, J. A.; Takahashi, Y.; Nakamura, K. Water-Gas-Shift Reaction on a $Ni_2P(001)$ Catalyst: Formation of Oxy-Phosphides and Highly Active Reaction Sites. *J. Catal.* **2009**, *262*, 294−303.

(7) Liu, X.; Chen, J.; Zhang, J. Hydrodechlorination of Chlorobenzene Over Silica-Supported Nickel Phosphide Catalysts. *Ind. Eng. Chem. Res.* **2008**, *47*, 5362−5368.

(8) Laursen, A. B.; Patraju, K. R.; Whitaker, M. J.; Retuerto, M.; Sarkar, T.; Yao, N.; Ramanujachary, K. V.; Greenblatt, M.; Dismukes, G. C. Nanocrystalline $Ni_5P_4$: A Hydrogen Evolution Electrocatalyst of Exceptional Efficiency in Both Alkaline and Acidic Media. *Energy Environ. Sci.* **2015**, *8*, 1027−1034.

(9) Aronsson, B.; Lundstrøm, T.; Rundqvist, S. *Borides, Silicides, and Phosphides: A Critical Review of Their Preparation Properties, and Crystal Chemistry*; Methuen: London, 1965.

(10) Corbridge, D. E. C. *Studies in Inorganic Chemistry*, 4th ed.; Elsevier: Amsterdam, Netherlands, 1990; Vol. *10*.

(11) Edamoto, K.; Nakadai, Y.; Inomata, H.; Ozawa, K.; Otani, S. Soft X-ray Photoelectron Spectroscopy Study of $Ni_2P$ (0001). *Solid State Commun.* **2008**, *148*, 135−138.

(12) Falch, S.; Lamparter, P.; Steeb, S. X-Ray Emission and Absorption Spectroscopy with Binary Amorphous Alloys from the B-Co-, B-Ni-, Co-P-, Co-Ti-, Cu-Mg-, Cu-Ti-, Mg-Zn-, Ni-P-, and Ni-Ti-Systems. *Z. Naturforsch., A: Phys. Sci.* **1984**, *39a*, 1175−1183.

(13) Kanama, D.; Oyama, S. T.; Otani, S.; Cox, D. F. Photoemission and LEED Characterization of $Ni_2P$ (0001). *Surf. Sci.* **2004**, *552*, 8−16.

(14) Li, Q.; Hu, X. First-Principles Study of $Ni_2P$ (0001) Surfaces. *Phys. Rev. B: Condens. Matter Mater. Phys.* **2006**, *74*, 035414.

(15) Moula, M. G.; Suzuki, S.; Chun, W.-J.; Otani, S.; Oyama, S. T.; Asakura, K. Surface Structures of $Ni_2P$ (0001)-Scanning Tunneling Microscopy (STM) and Low-Energy Electron Diffraction (LEED) Characterizations. *Surf. Interface Anal.* **2006**, *38*, 1611−1614.

(16) Suzuki, S.; Moula, G. M.; Miyamoto, T.; Nakagawa, Y.; Kinosthita, K.; Asakura, K.; Oyama, S. T.; Otani, S. Scanning Tunneling Microscopy and Photoemission Electron Microscopy Studies on Single Crystal $Ni_2P$ Surfaces. *J. Nanosci. Nanotechnol.* **2009**, *9*, 195−201.

(17) Kinoshita, K.; Simon, G. H.; König, T.; Heyde, M.; Freund, H.-J.; Nakagawa, Y.; Suzuki, S.; Chun, W.-J.; Oyama, S. T.; Otani, S.; Asakura, K. A Scanning Tunneling Microscopy Observation of $(\sqrt{3} \times \sqrt{3})$ $R30°$ Reconstructed $Ni_2P(0001)$. *Jpn. J. Appl. Phys.* **2008**, *47*, 6088.

(18) Hohenberg, P.; Kohn, W. Inhomogeneous Electron Gas. *Phys. Rev.* **1964**, *136*, B864.

(19) Kohn, W.; Sham, L. J. Self-Consistent Equations Including Exchange and Correlation Effects. *Phys. Rev.* **1965**, *140*, A1133.

(20) Giannozzi, P.; Baroni, S.; Bonini, N.; Calandra, M.; Car, R.; Cavazzoni, C.; Ceresoli, D.; Chiarotti, G. L.; Cococcioni, M.; Dabo, I.; Dal Corso, A.; de Gironcoli, S.; Fabris, S.; Fratesi, G.; Gebauer, R.; et al. QUANTUM ESPRESSO: A Modular and Open-Source Software Project for Quantum Simulations of Materials. *J. Phys.: Condens. Matter* **2009**, *21*, 395502.

(21) Perdew, J. P.; Burke, K.; Ernzerhof, M. Generalized Gradient Approximation Made Simple. *Phys. Rev. Lett.* **1996**, *77*, 3865.

(22) Rappe, A. M.; Rabe, K. M.; Kaxiras, E.; Joannopoulos, J. D. Optimized Pseudopotentials. *Phys. Rev. B: Condens. Matter Mater. Phys.* **1990**, *41*, 1227.

(23) Ramer, N. J.; Rappe, A. M. Designed Nonlocal Pseudopotentials for Enhanced Transferability. *Phys. Rev. B: Condens. Matter Mater. Phys.* **1999**, *58*, 12471−12478.

(24) Opium - pseudopotential generation project. http://opium.sourceforge.net.

(25) Bengtsson, L. Dipole Correction for Surface Supercell Calculations. *Phys. Rev. B: Condens. Matter Mater. Phys.* **1999**, *59*, 12301.

(26) Larsson, E. An X-ray Investigation of Ni-P System and Crystal Structures of NiP and $NiP_2$. *Ark. Kemi* **1965**, *23*, 335−365.

(27) Hernandez, A. B.; Ariga, H.; Takakusagi, S.; Kinoshita, K.; Suzuki, S.; Otani, S.; Oyama, S. T.; Asakura, K. Dynamical LEED Analysis of $Ni_2P$ (0001)-1 × 1: Evidence of P-Covered Surface Structure. *Chem. Phys. Lett.* **2011**, *513*, 48−52.

(28) Guo, D.; Nakagawa, Y.; Ariga, H.; Suzuki, S.; Kinoshita, K.; Miyamoto, T.; Takakusagi, S.; Asakura, K.; Otani, S.; Oyama, S. T. STM Studies on the Reconstruction of the $Ni_2P(10\bar{1}0)$ Surface. *Surf. Sci.* **2010**, *604*, 1347−1352.

(29) Liu, P.; Rodriguez, J. A. Catalysts for Hydrogen Evolution from the [NiFe] Hydrogenase to the $Ni_2P$ (001) Surface: The Importance of Ensemble Effect. *J. Am. Chem. Soc.* **2005**, *127*, 14871−14878.

(30) Ariga, H.; Kawashima, M.; Takakusagi, S.; Asakura, K. Density Functional Theoretical Investigation on the $Ni_3PP$ Structure and the Hydrogen Adsorption Property of the $Ni_2P(0001)$ Surface. *Chem. Lett.* **2013**, *42*, 1481−1483.

(31) Liu, P.; Rodriguez, J. A.; Asakura, T.; Gomes, J.; Nakamura, K. Desulfurization Reactions on $Ni_2P(001)$ and $\alpha$-$Mo_2C(001)$ Surfaces: Complex Role of P and C Sites. *J. Phys. Chem. B* **2005**, *109*, 4575−4583.

(32) Kanama, D.; Oyama, S. T.; Otani, S.; Cox, D. F. $Ni_2P(0001)$ by XPS. *Surf. Sci. Spectra* **2001**, *8*, 220−224.

(33) Moon, J. S.; Kim, E. G.; Lee, Y. K. Active Sites of $Ni_2P/SiO_2$ Catalyst for Hydrodeoxygenation of Guaiacol: A Joint XAFS and DFT Study. *J. Catal.* **2014**, *311*, 144−152.

(34) Maxwell, L. R.; Hendricks, S. B.; Mosley, V. M. Electron Diffraction by Gases. *J. Chem. Phys.* **1935**, *3*, 699−709.

(35) Hellwege, K. H.; Hellwege, A. M. *Atomic and Molecular Physics*; Landolt-Bornstein: Berlin, 1976.

(36) Saidi, W. A.; Martirez, J. M. P.; Rappe, A. M. Strong Reciprocal Interaction Between Polarization and Surface Stoichiometry in Oxide Ferroelectrics. *Nano Lett.* **2014**, *14*, 6711−6717.

(37) Kim, S.; Sinai, O.; Lee, C. W.; Rappe, A. M. Controlling Oxide Surface Dipole and Reactivity with Intrinsic Nonstoichiometric Epitaxial Reconstructions. *Phys. Rev. B: Condens. Matter Mater. Phys.* **2015**, *92*, 235431.



DOI: 10.1021/acs.chemmater.6b01437
*Chem. Mater.* 2016, 28, 5365−5372

(38) Levchenko, S. V.; Rappe, A. M. Influence of Ferroelectric Polarization on the Equilibrium Stoichiometry of Lithium Niobate (0001) Surfaces. *Phys. Rev. Lett.* **2008**, *100*, 256101.
(39) Morales, E. H.; Martirez, J. M. P.; Saidi, W. A.; Rappe, A. M.; Bonnell, D. A. Coexisting Surface Phases and Coherent One-Dimensional Interfaces on $BaTiO_3$ (001). *ACS Nano* **2014**, *8*, 4465−4473.
(40) Kolpak, A. M.; Li, D.; Shao, R.; Rappe, A. M.; Bonnell, D. A. Evolution of the Structure and Thermodynamic Stability of the $BaTiO_3$ (001) Surface. *Phys. Rev. Lett.* **2008**, *101*, 036102.
(41) Martirez, J. M. P.; Morales, E. H.; Saidi, W. A.; Bonnell, D. A.; Rappe, A. M. Atomic and Electronic Structure of the $BaTiO_3$(001) (5 × 5)*R*26.6° Surface Reconstruction. *Phys. Rev. Lett.* **2012**, *109*, 256802.
(42) Reuter, K.; Scheffler, M. Composition, Structure, and Stability of $RuO_2$(110) as a Function of Oxygen Pressure. *Phys. Rev. B: Condens. Matter Mater. Phys.* **1935**, *65*, 035406.



DOI: 10.1021/acs.chemmater.6b01437
*Chem. Mater.* 2016, 28, 5365−5372